



# Spray Coating Experiments: Setups and Methodologies



**The latest eBook from  
Advanced Optical Metrology.  
Download for free.**

*Spray Coating Experiments: Setups and Methodologies*, is the third in our Thin Films eBook series. This publication provides an introduction to spray coating, three article digests from Wiley Online Library and the latest news about Evident's Image of the Year Award 2022.

Wiley in collaboration with Evident, are committed to bridging the gap between fundamental research and industrial applications in the field of optical metrology. We strive to do this by collecting and organizing existing information, making it more accessible and useful for researchers and practitioners alike.

**EVIDENT**  
**OLYMPUS**

**WILEY**

# Bottom-Up Design of a Green and Transient Zinc-Ion Battery with Ultralong Lifespan

Neeru Mittal, Alazne Ojanguren, Dipan Kundu,\* Erlantz Lizundia,\* and Markus Niederberger\*

Transient batteries are expected to lessen the inherent environmental impact of traditional batteries that rely on toxic and critical raw materials. This work presents the bottom-up design of a fully transient Zn-ion battery (ZIB) made of nontoxic and earth-abundant elements, including a novel hydrogel electrolyte prepared by cross-linking agarose and carboxymethyl cellulose. Facilitated by a high ionic conductivity and a high positive zinc-ion species transference number, the optimized hydrogel electrolyte enables stable cycling of the Zn anode with a lifespan extending over 8500 h for  $0.25 \text{ mA cm}^{-2}$  –  $0.25 \text{ mAh cm}^{-2}$ . On pairing with a biocompatible organic polydopamine-based cathode, the full cell ZIB delivers a capacity of  $196 \text{ mAh g}^{-1}$  after 1000 cycles at a current density of  $0.5 \text{ A g}^{-1}$  and a capacity of  $110 \text{ mAh g}^{-1}$  after 10 000 cycles at a current density of  $1 \text{ A g}^{-1}$ . A transient ZIB with a biodegradable agarose casing displays an open circuit voltage of 1.123 V and provides a specific capacity of  $157 \text{ mAh g}^{-1}$  after 200 cycles at a current density of  $50 \text{ mA g}^{-1}$ . After completing its service life, the battery can disintegrate under composting conditions.

implementation of widespread approaches for renewable energy generation,<sup>[1]</sup> and mass-scale adoption of electric vehicles.<sup>[2]</sup> Such a green transition is only possible if efficient and environmentally friendly energy storage systems are developed.<sup>[1–3]</sup> As the most prominent and versatile energy storage system, batteries are anticipated to be the vital cog for the storage/delivery of on-demand power in an environmentally and socioeconomically sustainable manner.<sup>[4]</sup> Ideally, a sustainable energy storage device should deliver large capacities, present good rate capability, have long operating lifespans, and, most importantly, rely on nontoxic and noncritical materials.<sup>[5–7]</sup> These stringent requirements displace lithium ion batteries (LIBs) as the preferred choice for truly green batteries.<sup>[5]</sup> Current LIBs use toxic and flammable chemicals in the electrolyte (lithium hexafluorophosphate,

carbonate esters) and elements listed by the European Union as critical raw materials (CRMs), including cobalt, lithium, or graphite.<sup>[8,9]</sup> Besides their high supply risk with primary resources in Bolivia, Argentina, Chile, Australia, and the Democratic Republic of Congo, the disposal and subsequent marine/landfill accumulation of CRMs seriously threaten animal and

## 1. Introduction

The demand for sustainable and environmentally friendly solutions to reverse global warming and protect the biosphere has never been so urgent. Consequently, there is now a tremendous thrust to minimize fossil fuel dependency through the


N. Mittal, A. Ojanguren, M. Niederberger  
Laboratory for Multifunctional Materials  
Department of Materials  
ETH Zürich  
Vladimir-Prelog-Weg 5, Zurich 8093, Switzerland  
E-mail: markus.niederberger@mat.ethz.ch

D. Kundu  
LBRI, School of Chemical Engineering  
UNSW Sydney  
Kensington, NSW 2052, Australia  
E-mail: d.kundu@unsw.edu.au

D. Kundu  
School of Mechanical and Manufacturing Engineering  
UNSW Sydney  
Kensington, NSW 2052, Australia

E. Lizundia  
Life Cycle Thinking Group  
Department of Graphic Design and Engineering Projects  
Faculty of Engineering in Bilbao. University of the Basque Country (UPV/EHU)  
Bilbao 48013, Spain  
E-mail: erlantz.liizundia@ehu.eus

E. Lizundia  
BCMaterials  
Basque Center for Materials  
Applications and Nanostructures  
UPV/EHU Science Park, Leioa 48940, Spain

 The ORCID identification number(s) for the author(s) of this article can be found under <https://doi.org/10.1002/smll.202206249>.

© 2022 The Authors. Small published by Wiley-VCH GmbH. This is an open access article under the terms of the Creative Commons Attribution-NonCommercial License, which permits use, distribution and reproduction in any medium, provided the original work is properly cited and is not used for commercial purposes.

DOI: 10.1002/smll.202206249

human health.<sup>[10]</sup> Even assuming a favorable scenario in which most LIBs are recycled (currently recycling rate is approximately 2–5%),<sup>[11]</sup> harmful substances are created during recycling. If no viable alternatives are developed, these issues will become more severe as the demand for lithium and cobalt is expected to increase by 15 and 60 times, respectively, by 2030.<sup>[8]</sup>

Multivalent ion-based batteries are a promising alternative to developing sustainable secondary batteries because the corresponding metallic anodes (e.g., Mg, Al, Zn) are available in large quantities and promise high gravimetric and volumetric energy densities.<sup>[12]</sup> The Zn-ion chemistry is particularly exciting as it employs an earth-abundant Zn metal anode and near-neutral aqueous electrolytes,<sup>[13,14]</sup> which make the batteries safe, inexpensive, and environmentally benign. Furthermore, the high ionic conductivities (up to  $1 \text{ S cm}^{-1}$ ) of aqueous electrolytes allow rapid (dis)charge rates.<sup>[13]</sup> As opposed to Li, metallic Zn can be recycled indefinitely in an open atmosphere with no changes in its physical properties,<sup>[14]</sup> and the electrolyte salt (e.g.,  $\text{ZnSO}_4$ ) can be easily separated and reused.<sup>[15]</sup> With such characteristics, Zn-ion batteries (ZIBs) are ideal for developing truly environmentally friendly batteries. However, for their practical application, the cyclability of the Zn anode, which suffers from rapid dendritic failure, and the sluggish solid-state diffusion of  $\text{Zn}^{2+}$  at the cathode, need to be improved.<sup>[16]</sup> Although several elegant approaches have already dealt with these inconveniences,<sup>[17]</sup> those used toxic or nondegradable materials, limiting the full exploitation of the inherent environmental benefits of ZIBs.

A significant achievement in the promotion of sustainable energy storage systems can potentially arise from developing transient secondary batteries. Transient batteries can be disintegrated, dissolved, or degraded into nontoxic products after a period of reliable operation.<sup>[18]</sup> Accordingly, they represent a viable solution to circumvent the accumulation of long-lasting and hazardous battery waste dumped into marine and land environments, considered as one of the major global environmental issues.<sup>[19]</sup> However, the design of transient batteries faces severe challenges due to the limited choice of degradable and nontoxic materials.<sup>[18]</sup> As a result, developing transient batteries with competitive electrochemical performances remains a daunting task.

We took up this challenge and developed a transient ZIB that delivers an electrochemical performance similar to traditional batteries in terms of capacity and cycle life while still exhibiting excellent degradability. To achieve this, we replace the conventional glass fiber separator, widely used in ZIBs, with a cross-linked agarose/carboxymethyl cellulose hydrogel electrolyte.<sup>[20]</sup> The hydrogel electrolyte enables a lifespan of more than 4000 h for the Zn anode, eliminating the anode reversibility and stability concerns of ZIBs. This is particularly significant considering that most other notable approaches involve toxic electrolyte additives (triethyl phosphate),<sup>[21]</sup> petroleum-based materials (polyethyleneimine,<sup>[22]</sup> polyamide),<sup>[23]</sup> or inorganic metal oxide nanoparticles.<sup>[24]</sup> Additionally, the severely limited  $\text{Zn}^{2+}$  diffusion inside inorganic hosts is resolved by applying an organic cathode composed of polydopamine (PDA), which has remarkable redox activity and biocompatible character.<sup>[25]</sup> Careful tuning of the PDA cathode enables a full ZIB cell that displays a high capacity and excellent long-term cyclability.

A thin (around  $25 \mu\text{m}$ ) agarose encasing protects the internal components during operation and allows degradation under composting conditions, resulting in a truly transient battery.

## 2. Results and Discussion

### 2.1. Biopolymer-Derived Hydrogel Electrolyte

The development of a biodegradable electrolyte is key to constructing a fully transient ZIB. The inherent ability of polysaccharides to retain a large volume of aqueous electrolyte within their solid structure without dissolving can allow rapid ionic transport (i.e., high ionic conductivity) while maintaining geometrical stability.<sup>[26]</sup> Besides, polysaccharides are renewable, widely available, inexpensive, and their degradation products do not impart toxic responses.<sup>[27]</sup> Previously, our group demonstrated the ability of agarose (AG)<sup>[28]</sup> and carboxymethyl cellulose (CMC),<sup>[29]</sup> to enable stable and homogeneous alkali metal deposition with restricted dendrite growth. While AG shows enhanced hydrophilicity because of its many  $-\text{OH}$  groups, CMC offers good mechanical properties. Therefore, we explored the suitability of AG and CMC mixtures to develop hydrogel electrolytes for ZIBs. To facilitate gel formation and provide the electrolyte film with enough mechanical stability, glutaraldehyde was used as a chemical crosslinker.<sup>[30]</sup> The mixture bearing glutaraldehyde, AG, CMC, and water at different concentrations was left to react for 1 h at  $80^\circ\text{C}$ , and after pouring the solution into a Petri-dish, the solution was dried at room temperature for 72 h (Figure S1, Supporting Information). A concentration of 4 wt% glutaraldehyde was found to be most suitable for balancing gel-forming capacity and processability. Lower concentrations resulted in flowing materials, while higher concentrations yielded high viscosities, making processing difficult. Hydrogel electrolytes were then obtained by soaking the dried, self-supporting films in an aqueous 2 M  $\text{ZnSO}_4$  solution. Naked-eye observations in Figure S2 (Supporting Information) indicate that AG:CMC hydrogel electrolytes retain their shape, while the pure CMC hydrogel suffers from the dissolution of the cellulose. Accordingly, only AG:CMC ratios of 100:0, 75:25, 50:50, and 25:75 were investigated.

The cross-sectional morphology of the freeze-dried hydrogel electrolytes is shown in Figure 1. Despite their rough surface, no phase-separation is observed that would be evident from the typical sea-island morphology,<sup>[31]</sup> indicating the successful formation of miscible polymeric blends. While 100:0 and 75:25 samples do not show any macroporosity, 50:50 and 25:75 compositions display abundant interconnected pores of nearly  $10 \mu\text{m}$  in diameter. Upon soaking, these pores offer increased surface area and uphold large amounts of liquid, critical for uniform ion transport throughout the whole structure.<sup>[32]</sup>

Attenuated total reflectance-Fourier transform infrared (ATR-FTIR) spectroscopy was applied to study any potential specific interactions between AG and CMC. The spectra in Figure 2a are characterized by a broad absorption band in the  $3600\text{--}3000 \text{ cm}^{-1}$  range arising from  $-\text{OH}$  stretching and intra/intermolecular hydrogen bonds in both polysaccharides, with an additional sharp band around  $1060\text{--}1072 \text{ cm}^{-1}$  originating from either the C–O groups in agarose,<sup>[28]</sup> or the  $\text{CH-O-CH}_2$



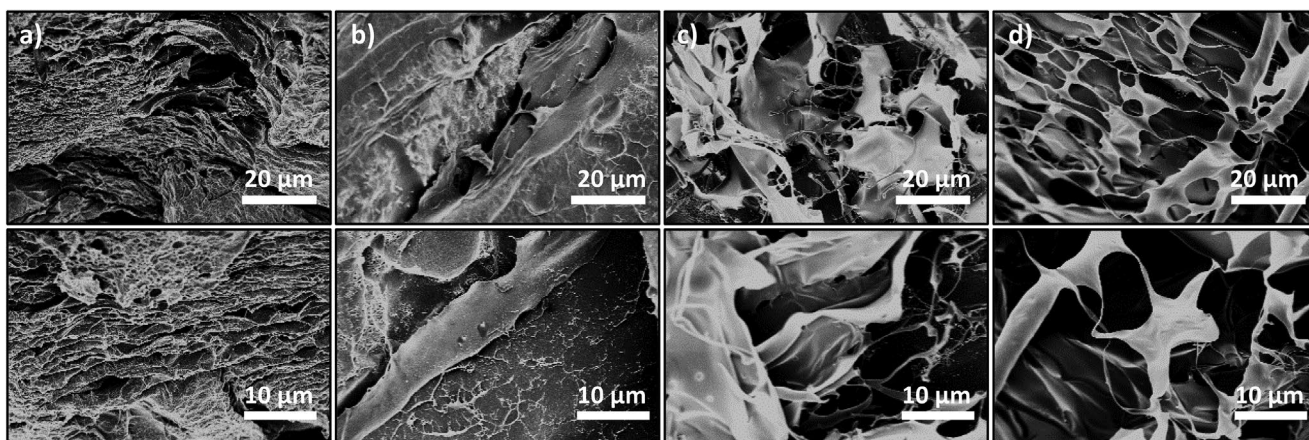


**Figure 1.** Representative SEM micrographs showing the cross-sectional morphology of freeze-dried agarose (AG):carboxymethyl cellulose (CMC) hydrogel electrolytes at weight ratios of a) 100:0, b) 75:25, c) 50:50, and d) 25:75.

stretching of CMC.<sup>[33]</sup> While the intensity of the C–H stretching band at 3000–2800  $\text{cm}^{-1}$  of the agarose alkane group decreases with increasing CMC concentration, new peaks emerge at 1427 and 1340  $\text{cm}^{-1}$  due to the  $-\text{CH}_2$  scissoring and  $-\text{OH}$  bending vibrations of CMC.<sup>[33]</sup> Interestingly, the position of the bands at 3600–3000  $\text{cm}^{-1}$  and  $\approx 1065 \text{ cm}^{-1}$  shifts to lower wavenumbers by 155 and 63  $\text{cm}^{-1}$ , respectively, for blended compositions, indicating significant interactions between AG and CMC via hydrogen bonding.<sup>[31]</sup> These results confirm the formation of

a polymeric network homogeneously mixed at the molecular level, which is considered a prime requisite for the development of hydrogel electrolytes with high ionic conductivities.<sup>[34]</sup> This finding is consistent with previous reports on thermodynamically miscible sodium alginate and CMC blends.<sup>[35]</sup>

X-ray diffraction patterns in Figure 2b show a main broad peak centered at  $2\theta = 18.8^\circ$  and a shoulder at  $2\theta = 36\text{--}45^\circ$  characteristic of the polysaccharide rings in agarose,<sup>[36]</sup> corroborating the predominantly amorphous character of the hydrogel.

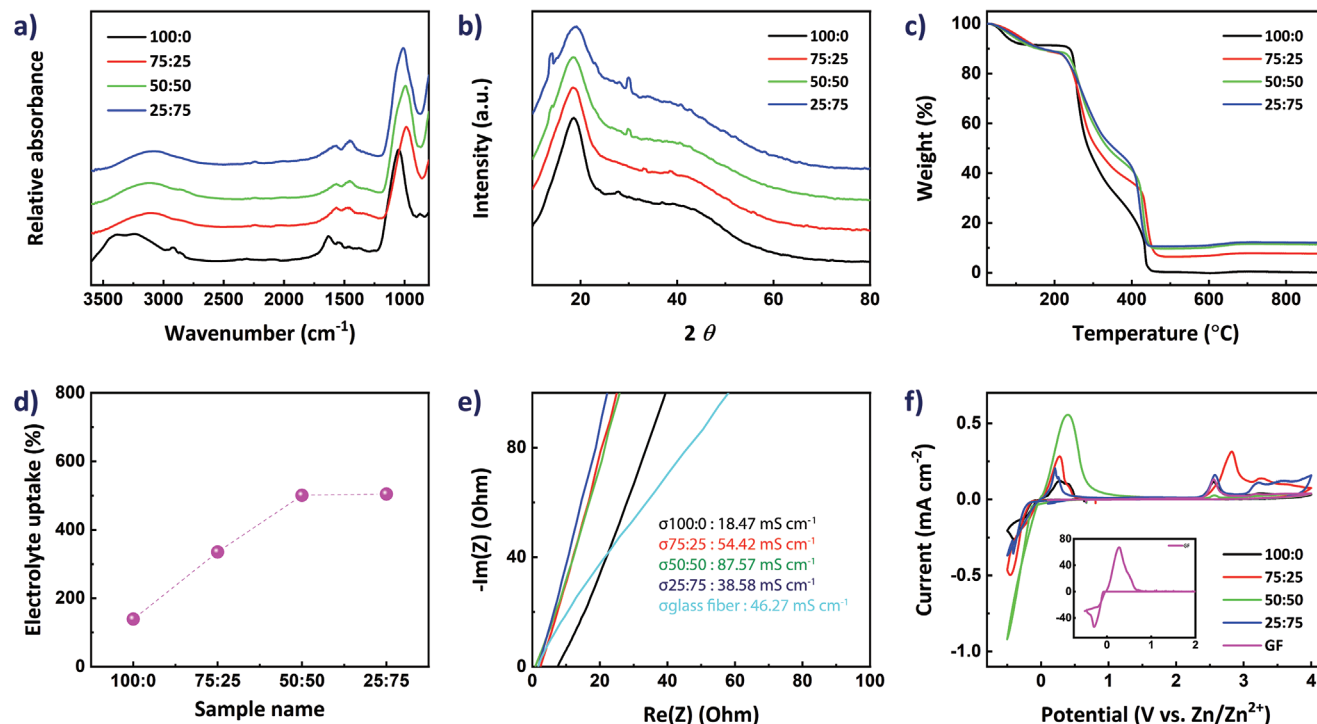


**Figure 2.** a) Attenuated total reflectance-Fourier transform infrared (ATR-FTIR) spectra. b) XRD patterns of agarose (AG):carboxymethyl cellulose (CMC) (AG:CMC) hydrogel electrolytes. c) TGA curves of different concentrations of agarose and CMC polymer blends measured in the air; d) electrolyte uptake (EU); and e) Nyquist impedance plots of AG:CMC hydrogel electrolytes. For comparison, the impedance plot of a glass fiber separator soaked in 2 M  $\text{ZnSO}_4$  is also shown. f) Electrochemical stability window of AG:CMC hydrogel electrolytes. The inset shows the electrochemical stability of the glass fiber separator expanded in the  $-0.5$  to 2 V window versus  $\text{Zn}/\text{Zn}^{2+}$ .

No additional peaks are observed upon CMC incorporation, but its diffraction peaks at  $2\theta = 10^\circ$  and  $20.0^\circ$  would anyway overlap with the agarose pattern.<sup>[37]</sup> Importantly, no peaks attributed to crystalline  $\text{ZnSO}_4$  are identified, indicating that the zinc salt is fully dissociated. This is very important as sulfate salts tend to precipitate out when incorporated into polymers such as polyethylene glycol, or polyvinyl alcohol.<sup>[38]</sup> The enhanced salt dissociation originates from the dielectric properties of AG and CMC, which both act as a polyelectrolyte in the presence of water, indicating an enhanced  $\text{Zn}^{2+}$  conductivity through the AG:CMC hydrogel electrolytes.<sup>[39]</sup> The thermal stability of the AG:CMC blends was assessed by thermogravimetric analysis. As shown in Figure 2c, a 9 wt% mass loss occurs at temperatures between  $50^\circ\text{C}$  and  $140^\circ\text{C}$  due to dehydration of the highly hygroscopic polysaccharides.<sup>[40]</sup> A two-step degradation process is observed for neat agarose in the temperature range of  $250\text{--}300^\circ\text{C}$  and  $430\text{--}450^\circ\text{C}$ , in accordance with previous results.<sup>[28]</sup> The thermal stability increases with the CMC content, shifting the second degradation step to higher temperatures by  $10\text{--}15^\circ\text{C}$ . CMC degradation proceeds through decarboxylation of the carboxylic groups into  $\text{CO}_2$ , resulting in aromatized units that eventually decompose into a cross-linked carbon skeleton.<sup>[41]</sup> With the main degradation step centered at  $\approx 340^\circ\text{C}$ , the cross-linked AG and CMC gel shows an enhanced thermal stability over Celgard, which degrades in the  $280\text{--}320^\circ\text{C}$  range. This superior thermal stability over separators based on pure petrochemical resources offers a reduced likelihood of thermal runaway.

The highly porous structure of the freeze-dried AG:CMC hydrogel electrolytes, as already observed in SEM, is also confirmed by the  $\text{N}_2$  adsorption–desorption isotherms in Figure S3 (Supporting Information). The Brunauer–Emmett–Teller (BET) surface area ranges from  $48.0\text{ m}^2\text{ g}^{-1}$  for neat CMC to  $139.4\text{ m}^2\text{ g}^{-1}$  for the 75:25 sample (pore volumes of  $0.081$  to  $0.294\text{ cm}^3\text{ g}^{-1}$ ). The specific surface area decreases with increasing fraction of CMC (from  $128.2\text{ m}^2\text{ g}^{-1}$  for neat agarose to  $48.0\text{ m}^2\text{ g}^{-1}$  for the 25:75 sample). Thus, the lower the CMC fraction, the more oxygen-containing functional groups are available to interact with  $\text{Zn}^{2+}$ , which indirectly boosts the ionic conductivity. These values are also significantly larger than the  $10.8\text{ m}^2\text{ g}^{-1}$  obtained for the glass fiber separator.<sup>[28]</sup> This large porosity, together with the polarity provided by the  $-\text{O}-$ ,  $-\text{OH}$ , and  $-\text{C}=\text{O}$  functional groups of the polymer membranes, is ideal for holding a large volume of the aqueous electrolyte. Therefore, the electrolyte uptake (EU) of AG:CMC films in  $2\text{ M ZnSO}_4$  aqueous solution was measured based on Equation S1 (Supporting Information). As summarized in Figure 2d, the EU value increases with CMC concentration, reaching  $139.1\text{ wt}\%$  for neat agarose to a maximum of  $504.3\text{ wt}\%$  for the 25:75 sample. For pure CMC, the EU value exceeded  $1000\text{ wt}\%$ , but the film then got fully dissolved. These large values arise from the combined effect of many oxygen-containing polar groups of the polysaccharides and the capillary action enabled by the pores.<sup>[42]</sup> The effect of the large EU values on efficient  $\text{Zn}^{2+}$  transport through the hydrogels was confirmed by the room temperature ionic conductivity measurement (Figure 2e; Equation S2, Supporting Information). The 50:50 hydrogel electrolyte exhibits the highest room-temperature ionic conductivity of  $87.57 \times 10^{-3}\text{ S cm}^{-1}$ , which is more than twice that of the liquid electrolyte, while 100:0, 75:25, and

25:75 compositions also possess high values of 18.47, 54.42, and  $38.58 \times 10^{-3}\text{ S cm}^{-1}$ , respectively. These values exceed those reported for the lignin/Nafion separator soaked in  $2\text{ M ZnSO}_4$  aqueous solution ( $9.1 \times 10^{-3}\text{ S cm}^{-1}$ ),<sup>[43]</sup> a gel polymer electrolyte (GPE) based on  $3\text{ M ZnSO}_4/0.1\text{ M MnSO}_4/20\text{ wt}\%$  xanthan gum ( $16.5 \times 10^{-3}\text{ S cm}^{-1}$ ),<sup>[44]</sup> and a cellulose nanofiber GPE ( $16.4 \times 10^{-3}\text{ S cm}^{-1}$ ).<sup>[45]</sup>

The strong affinity of the abundant oxygen groups in agarose and CMC for the aqueous phase facilitates the rapid movement of hydrated ions through the ion channels of the hydrogel, leading to the very high ionic conductivity observed here.<sup>[43]</sup> However, a significant contribution of the  $\text{Zn}^{2+}$  transport to the total ionic conductivity is critical to minimize polarization losses and, in particular, to inhibit dendritic zinc deposition resulting from the ionic concentration gradient at high current densities.<sup>[46]</sup> Therefore, the AG:CMC hydrogel electrolytes were further investigated to determine the zinc-ion transference number.<sup>[47,48]</sup> The 50:50 hydrogel electrolyte displays the highest and a net positive zinc-ion species transference number (Table S1, Supporting Information) compared to a significantly negative value observed for the liquid electrolyte. Negative transference numbers often arise due to the formation of cation–anion pairs in concentrated electrolytes and migration of the active ion (zinc-ion) species in the “wrong” direction (see discussion in the Supporting Information).<sup>[49]</sup> A net negative zinc transference number is expected to lead to the depletion of the ion concentration at the electrode–electrolyte interface at even moderate current densities, triggering ramified zinc deposition. In contrast, the hydrogel electrolytes, particularly the 50:50 electrolyte, are expected to support higher current densities, enabling dendrite-free zinc deposition, thanks to the favorable transport property. Considering all the advantageous properties such as porous morphology, predominantly amorphous structure, and remarkable ionic conductivity, the AG:CMC hydrogel electrolytes are expected to be excellent electrolytes in ZIBs. Accordingly, we studied their electrochemical stability by combining cyclic voltammetry and linear sweep voltammetry in an asymmetric Zn/Ti cell. Figure 2f shows the data in the  $-0.5$  to  $4.0\text{ V}$  window versus  $\text{Zn}/\text{Zn}^{2+}$ . The AG:CMC hydrogel electrolytes are highly stable up to  $2.3\text{ V}$ , making them suitable for a wide variety of cathode materials, including the high voltage materials developed for ZIBs.<sup>[50]</sup> On the cathodic side of the cyclic voltammogram, all hydrogel electrolytes enable reversible plating–stripping of Zn, which is fundamental for the stable operation of a Zn anode. It is important to note that the developed hydrogel electrolytes do not contain fluorinated anions, which can form toxic fluoro-organic compounds that could affect battery safety.<sup>[51]</sup>

Mechanically robust but deformable hydrogels possess ideal prerequisites for batteries with a long lifespan due to improved electrolyte–electrode compatibility.<sup>[52]</sup> The compressive properties of the hydrogels determine not only their ability to withstand external forces when used in batteries but also their resistance against dendrite piercing.<sup>[53]</sup> Accordingly, representative uniaxial compressive stress–strain curves of the AG:CMC hydrogel electrolytes in Figure S4 (Supporting Information) reveal that CMC addition improves the flexibility of the gel while keeping notably large compressive strength values of  $1066\text{ kPa}$  at  $40\%$  strain for the 50:50 hydrogel electrolyte ( $5027, 874, 2557\text{ kPa}$  for 100:0, 75:25, and 25:75 samples,

respectively). This value is well above that of other biopolymer hydrogels, which usually lie close to 250 kPa (for CNC hydrogels),<sup>[54]</sup> and 100–350 kPa for chemically dual-cross-linked cellulose hydrogels.<sup>[55]</sup> The compressive modulus of 1.14 MPa for 50:50 hydrogel electrolyte also reduces the possibility of a short circuit by preventing dendrite growth, thus enhancing both the battery safety and lifespan.<sup>[56]</sup> In comparison, even better compressive modulus values of 10.71, 1.29, and 3.79 MPa are obtained for 100:0, 75:25, and 25:75 samples, respectively. Such improved mechanical compressive response suggests that our electrolytes can withstand external forces when applied to

batteries. Additionally, this feature increases the ability of the highly porous polysaccharide network to accommodate external stresses without collapse, crack formation, or electrolyte loss.

The observed mechanical performance together with the large ionic conductivity lay the foundation for a uniform Zn<sup>2+</sup> transport across the electrolyte–Zn interface, necessary for a smooth charge and mass transfer with limited Zn dendrite growth.<sup>[44]</sup> Accordingly, reversibility of the zinc plating-stripping was probed by galvanostatic cycling in a symmetric Zn|Zn configuration. The polarization profiles correspond to 1 mA cm<sup>-2</sup> – 1 mAh cm<sup>-2</sup> symmetric Zn plating-stripping with

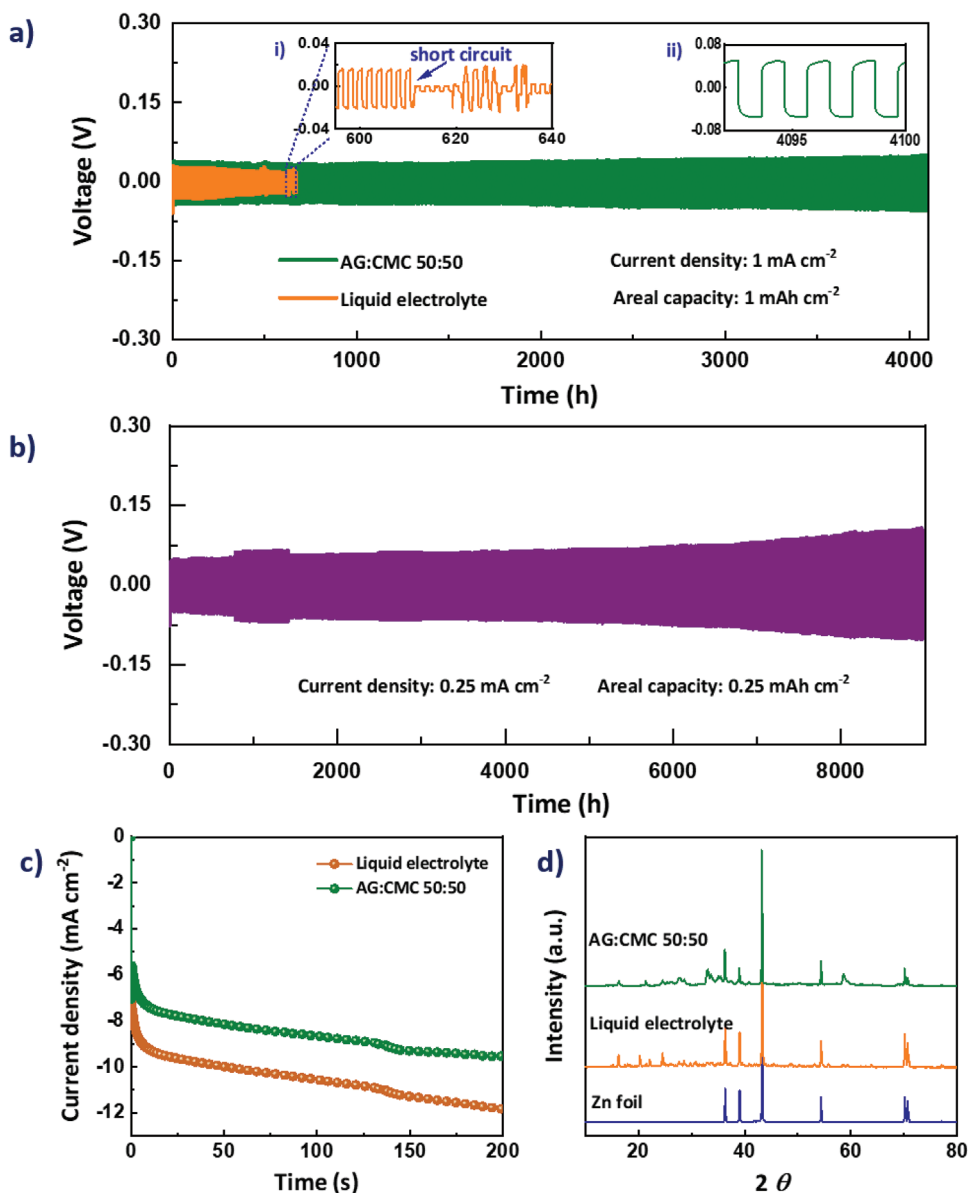


**Figure 3.** Room temperature voltage–time profiles for the symmetric Zn plating-stripping at a) 1 mA cm<sup>-2</sup> – 1 mAh cm<sup>-2</sup> and b) 0.25 mA cm<sup>-2</sup> – 0.25 mAh cm<sup>-2</sup> for agarose (AG):carboxymethyl cellulose (CMC) (AG:CMC) 50:50 hydrogel electrolyte. The data for a glass fiber separator soaked in a 2 M ZnSO<sub>4</sub> electrolyte solution, denoted as the liquid electrolyte, is also shown (orange) for comparison. The insets (i,ii) in Figure (a) show a magnified view of a short-circuit occurring in the liquid electrolyte system after 605 h and the polarization curves of the AG:CMC 50:50 hydrogel electrolyte in the time range of 4000 to 4100 h. c) Chronoamperograms (CAs) of Zn/Zn cell using AG:CMC 50:50 hydrogel or liquid electrolytes at an overpotential of –150 mV. d) Postmortem XRD analysis of the Zn foil after cycling with AG:CMC 50:50 hydrogel electrolyte or liquid electrolyte.



AG:CMC 50:50 hydrogel electrolyte compared with the regular 2 M ZnSO<sub>4</sub>·H<sub>2</sub>O are shown in Figure 3a. While the hydrogel electrolyte displays a remarkably stable voltage response with a relatively small polarization of 40 mV for over 4000 h (2000 cycles), the liquid electrolyte leads to short-circuit—as indicated by the sudden drop in polarization after 605 h only (302 cycles, Figure 3a, inset i)). The observed overpotential for the 50:50 hydrogel electrolyte remains well below the 80 mV reported for the polyacrylamide electrolyte widely used in flexible aqueous ZIBs (2 M ZnSO<sub>4</sub> + 4 M LiCl; 1 mA – 1 mAh cm<sup>-2</sup>).<sup>[57]</sup> As shown in inset ii) of Figure 3a, the voltage–time trace maintains a steady and flat shape over the whole time interval, in agreement with a stable and smooth zinc deposition–dissolution process. The demonstrated lifespan is superior to previously reported works which mainly involve nontransient strategies such as the use of petroleum-based gel electrolytes,<sup>[58]</sup> the use of strongly oxidizing, flammable, and hazardous electrolyte additives such as Zn(ClO<sub>4</sub>)<sub>2</sub>,<sup>[59]</sup> or anodes bearing complex materials such as Ti<sub>3</sub>C<sub>2</sub>T<sub>x</sub> MXene.<sup>[60]</sup>

Zn/Zn cell with 50:50 hydrogel electrolyte was additionally evaluated at 0.25 mA cm<sup>-2</sup> – 0.25 mAh cm<sup>-2</sup> (Figure 3b), resulting in excellent cycling stability of over 8500 h. Such a long-lasting cycling performance enabled by the hydrogel electrolyte can be primarily ascribed to the following reasons. First, the soft polymer of the hydrogel can form an intimate and seamless contact with the rough Zn foil. Second, the electrostatic interaction between the abundant electron donor atoms of AG:CMC hydrogel and zinc ionic species may allow a stable diffusion of zinc ions across the interface. Both these factors can induce a uniform deposition of zinc ions on the anode's surface, thus inhibiting dendrite growth. To understand the difference in the zinc deposition behavior when using the

liquid electrolyte and 50:50 hydrogel electrolyte, chronoamperometry (CA) measurements, as shown in Figure 3c, were carried out under an overpotential of –150 mV. The current–time profile in CA curves gives an indication of the nucleation and deposition process of Zn<sup>2+</sup> on the anode's surface. Compared with the liquid electrolyte, the current of the symmetric cell with hydrogel electrolyte is lower, suggesting a more controlled and uniform Zn<sup>2+</sup> deposition that results in a dendrite-free and smooth Zn electrode. As depicted in Figure 3d, the XRD indicates that Zn<sub>4</sub>(OH)<sub>6</sub>SO<sub>4</sub>·5H<sub>2</sub>O is the main corrosion product formed onto the Zn anode after a long-term cycling test for both liquid and hydrogel electrolytes. This byproduct is usually formed during the discharge process and appears in the form of small flakes.<sup>[23,61]</sup>

SEM was employed to further confirm that the stable Zn plating–stripping is indeed translated into a homogeneous and dendrite-free Zn deposition at the microscale. Figure 4 shows SEM images of the Zn metal surfaces after cycling in a symmetric Zn cell at 1 mA cm<sup>-2</sup> – 1 mAh cm<sup>-2</sup> using the traditional liquid electrolyte and the AG:CMC 50:50 hydrogel electrolyte. The pristine Zn foil (Figure 4a) is shown for comparison. A rough surface covered by flake-like deposits (Figure 4b) is observed when the liquid electrolyte is used, while for the hydrogel electrolyte, the surface is comparably smooth and homogeneous (Figure 4c). These results indicate that the hydrogel allows uniform diffusion of zinc ions, which ensures a steady current density across the anode–electrolyte interface during repeated cycling. The good interfacial compatibility imparted by the hydroxyl groups, the compliant nature of the hydrogel, and the high ionic conductivity (8757 × 10<sup>-3</sup> S cm<sup>-1</sup>) along with a positive zinc-ion species transference number, all contribute to the improved zinc anode cyclability.

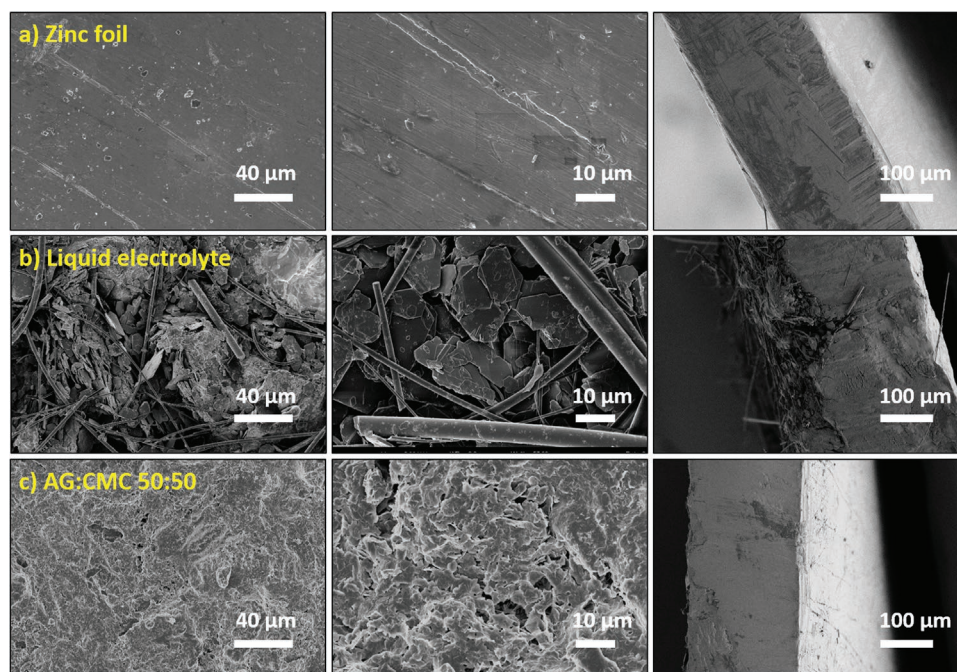


**Figure 4.** Top and cross-sectional SEM micrographs of the surface of the Zn metal at different magnifications: a) before galvanostatic cycling and after symmetric cycling at 1 mA cm<sup>-2</sup> – 1 mAh cm<sup>-2</sup> using b) liquid electrolyte and c) agarose (AG):carboxymethyl cellulose (AG:CMC) 50:50 hydrogel electrolyte.

## 2.2. Performance of the Polydopamine Cathode

Polydopamine (PDA), a bioderived material, has been well exploited as the cathode material for various rechargeable batteries, including ZIBs, due to its fast kinetics and high capacity.<sup>[62,63]</sup> It is readily obtained by oxidative polymerization of dopamine in a slightly alkaline environment and contains multiple redox sites that easily coordinate with metal ions. Thanks to its excellent adhesion, PDA can be applied to a multitude of surfaces, including organic, inorganic, and ceramic materials. Inspired by these properties, we synthesized PDA particles and characterized them using SEM and FTIR, and a detailed discussion is provided in the SI (Figure S5, Supporting Information). The as-obtained PDA particles were drop-cast onto a carbon cloth (CC), a textile current collector, yielding a cathode (CC/PDA particles) suitable for transient ZIBs. The CC current collector, despite being nondegradable, was selected since it is completely inert and nontoxic and provides good electrical conductivity of  $\approx 2$  S  $\text{cm}^{-1}$ . The ZIB containing CC/PDA particles electrode and traditional liquid electrolyte deliver a moderate discharge capacity of 100  $\text{mAh g}^{-1}$  during the first cycle but becomes irreversible thereafter (Figure 5a). A closer look at the SEM images of the cycled CC/PDA particles electrode revealed a morphological transformation of the spherical PDA particles into a dense film (Figure S6, Supporting Information). We assume that during this transformation, the detachment of the PDA particles from the CC can occur, resulting in an insufficient electrical contact between the transformed PDA particles and CC. This could be a possible reason for this poor performance; therefore, we polymerized PDA directly on the CC as the next step.

To facilitate the PDA coating on the hydrophobic CC with its low surface energy, an organic solvent based method with piperidine as the organic base was used to oxidize the catechol moieties.<sup>[64]</sup> During the polymerization process, the CC was immersed into the colorless ethanol solution containing dopamine and piperidine for a few hours, after which the solution turned dark brown, indicating the oxidation of dopamine molecules. The red-shift of the free dopamine peak at 280 nm to over 300 nm in the UV-Vis spectra confirms the dopamine polymerization (Figure S7, Supporting Information). We then investigated the surface morphology of the PDA polymerized on CC (CC/PDA) using SEM and compared it with the pristine CC (Figure S8, Supporting Information). After polymerization, the smooth CC surface is uniformly covered by a thin PDA layer. The PDA coating on CC is also confirmed by the color change from colorless to brown when CC/PDA is immersed in a 1 M sodium hydroxide solution (Figure S8, Supporting Information). No such color change is observed for the pristine CC. This indicates the dissolution of PDA in the strong basic environment, thus corroborating the presence of PDA on CC.<sup>[25]</sup> The CC/PDA electrode in ZIB shows a high discharge capacity of 345.4  $\text{mAh g}^{-1}$  at 0.3  $\text{A g}^{-1}$  after five activation cycles at a low current density. Such an activation step was performed for all the galvanostatic tests reported here. Even though the battery maintained a decent capacity of 129.6  $\text{mAh g}^{-1}$  after 400 cycles (Figure 5a), the fading is still significant. Therefore, to improve the capacity retention further, we coated the CC with a slurry of activated carbon prior to the PDA polymerization (CC-AC/PDA). This step turned out to be essential to increase the mass loading of the active polymer and improve the adhesion, which is necessary for rapid ion and electron transport.

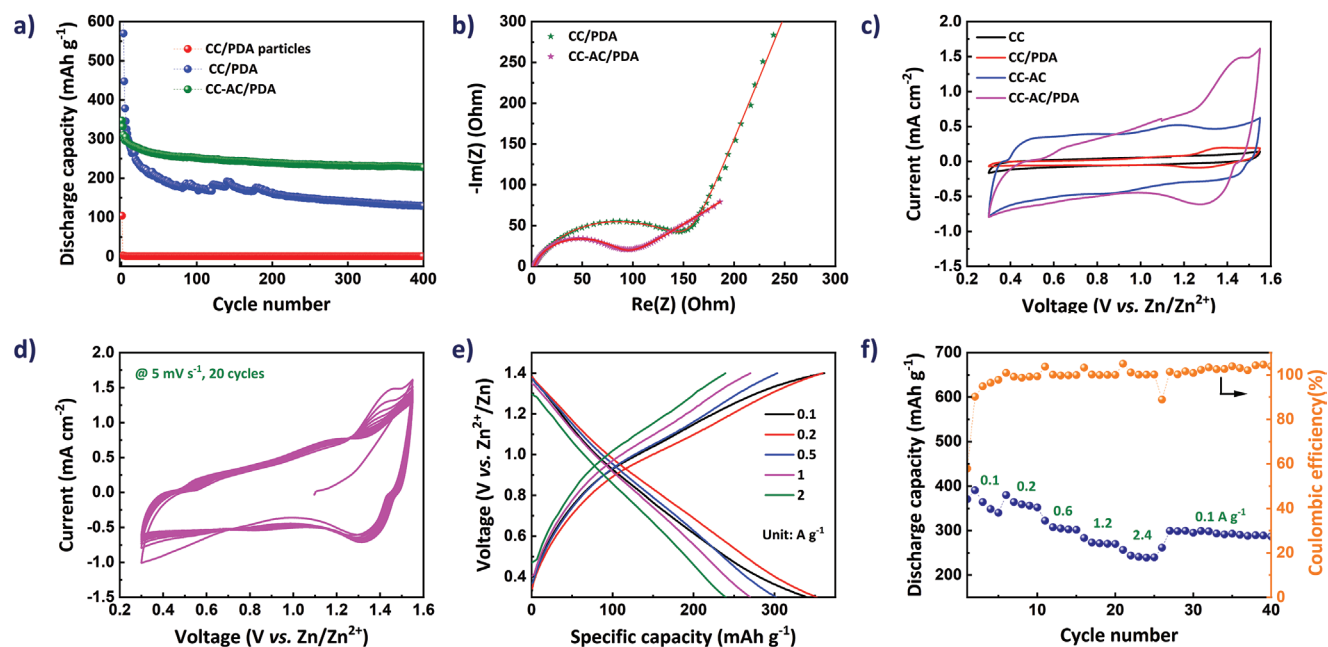


**Figure 5.** a) Galvanostatic cycling performance of the polydopamine (PDA) particles deposited on carbon cloth (CC/PDA particles), PDA polymerized on CC (CC/PDA), and PDA polymerized on activated carbon slurry-coated CC (CC-AC/PDA) performed at 0.3  $\text{A g}^{-1}$  in a ZIB with liquid electrolyte (glass fiber soaked in 2 M aqueous  $\text{ZnSO}_4$ ). b) EIS spectra of the CC/PDA and CC-AC/PDA electrodes and c) CV curves of CC, CC/PDA, CC-AC, and CC-AC/PDA electrodes in ZIBs at a scan rate of 5  $\text{mV s}^{-1}$ . Electrochemical characterization of CC-AC/PDA electrodes: d) CV curves for 20 cycles; e) galvanostatic charge–discharge curves at various current densities; and f) rate performance in ZIBs.



Like CC/PDA, the surface morphology of CC-AC after polymerization was studied using SEM, which showed a homogenous PDA coating, followed by the dissolution test in the basic environment (Figure S9, Supporting Information).<sup>[17]</sup> For such an electrode, we obtain an initial discharge capacity of 305.3 mAh g<sup>-1</sup> at a current density of 0.3 A g<sup>-1</sup>. After 100 cycles, 251.6 mAh g<sup>-1</sup> and after 400 cycles, 227.7 mAh g<sup>-1</sup> is retained. It is important to note that the capacity contribution of CC and CC-AC is negligible (Figure S10, Supporting Information). Furthermore, the activated carbon slurry coating process also results in improved charge transfer kinetics of the cathode, as shown in the Nyquist plots in Figure 5b.

The Nyquist plot is characterized by a semicircle in the middle frequency region representing the resistance to the charge transfer at the electrode–electrolyte interface ( $R_{CT}$ ) and a straight line in the low frequency region corresponding to diffusion impedance in the solid electrode. To quantify these parameters, an equivalent circuit was used to fit the impedance spectra and the results are summarized in Table S2 (Supporting Information). Compared to the  $R_{CT}$  value of 151.5  $\Omega$  for CC/PDA, a much lower value of 83.1  $\Omega$  is obtained for CC-AC/PDA, suggesting that the AC layer indeed favors an efficient ion transfer at the electrode–electrolyte interface. Cyclic voltammetry experiments were performed to get insights into the electrochemical behavior of various PDA-based electrodes. As shown in Figure 5c, CC-AC/PDA exhibits well-defined redox peaks with significantly higher current response than the other electrodes, pointing toward its excellent electroactivity. The CV profiles of CC-AC/PDA in Figure 5d nearly overlap after the initial activation cycles. Galvanostatic charge–discharge curves at various current densities for CC-AC/PDA are presented in Figure 5e, indicating the good rate kinetics. The excellent rate kinetics is also evident from the rate capability measurements shown in Figure 5f. Upon increasing the current density from 0.6 to 2.4 A g<sup>-1</sup>, the specific capacity drops by only 20% from 301.8 to 240.1 mAh g<sup>-1</sup>.

### 2.3. Transient ZIB

To evaluate the full cell performance, we first fabricated a fully rechargeable battery prototype using a zinc metal anode, CC-AC/PDA as cathode, and the AG:CMC 50:50 hydrogel electrolyte and tested it in the Swagelok-type configuration. The electrochemical performance as probed by galvanostatic cycling in the 0.3–1.4 V window (against the Zn anode) at a current density of 0.5 A g<sup>-1</sup> is shown in Figure 6a,b. A capacity of 264 mAh g<sup>-1</sup> is observed in the first cycle, which reduces to 211 mAh g<sup>-1</sup> after 100 cycles and 196.9 mAh g<sup>-1</sup> after 1000 cycles. The initial decrease in the capacity can be ascribed to the presence of unreacted dopamine and intermediate species that dissolve in the electrolyte. Although we did not use the traditional glass fiber separator and liquid electrolyte, our transient battery with the hydrogel electrolyte still delivers a comparable specific capacity of 264 versus 301 mAh g<sup>-1</sup>. The small decrease in specific capacity can be ascribed to the slightly higher resistance of the battery and the poor wettability of the cathode by the hydrogel electrolyte, as revealed by the EIS spectra presented in Figure 6c. The fitted impedance parameters in Table S2

(Supporting Information) show a reduced ohmic resistance value of 2.45  $\Omega$  for the liquid electrolyte in comparison to the 6.795  $\Omega$  observed for the hydrogel electrolyte. The rate performance of the zinc-ion battery with the hydrogel electrolyte is presented in Figure S11 (Supporting Information).

Additionally, the cycling performance in Figure 6d demonstrates a stability that is remarkable for a ZIB built of transient components, maintaining a discharge capacity of 110 mAh g<sup>-1</sup> after 10'000 cycles at a current density of 1 A g<sup>-1</sup>. Such a cycle life represents a big step forward toward the practical use of transient batteries in sustainable electronics. This becomes clear when we compare the performance of our batteries with the state-of-the-art transient primary and secondary batteries presented in the literature (compiled in Table S5, Supporting Information), including an Sn doped Li-V<sub>2</sub>O<sub>5</sub> battery delivering a capacity of 168 mAh g<sup>-1</sup> at 300 mA g<sup>-1</sup> for 200 cycles,<sup>[65]</sup> a Li-V<sub>2</sub>O<sub>5</sub> battery operating for four cycles only with 136 mAh g<sup>-1</sup> at 100 mA g<sup>-1</sup>,<sup>[66]</sup> a LiAl-V<sub>2</sub>O<sub>5</sub> battery lasting for 20 cycles with 200 mAh g<sup>-1</sup> at 1 A g<sup>-1</sup>,<sup>[67]</sup> or a Li-V<sub>2</sub>O<sub>5</sub> battery working for up to 400 cycles in ionic liquid electrolyte with a capacity of 30 mAh g<sup>-1</sup> at 100 mA g<sup>-1</sup>.<sup>[68]</sup>

The transiency of the battery was assessed by studying its disintegration under simulated aerobic composting conditions in a laboratory-scale test according to ISO 20200.<sup>[6]</sup> A fully transient rechargeable pouch cell was fabricated using a zinc metal anode, the AG:CMC 50:50 hydrogel electrolyte, and CC-AC/PDA cathode. Here, the choice of the packaging material for our transient ZIB is critical as the encasing ensures that the battery will only decompose under composting conditions, but not or very slowly under ambient conditions. Therefore, we developed an appropriate/versatile packaging using agarose, a neutral linear polysaccharide of marine origin that protects the battery against moisture, and gas permeation under conventional atmospheric conditions but easily decomposes in the compost.<sup>[28,69]</sup> The SEM image of the surface morphology and digital photographs of the highly transparent and flexible agarose casing are shown in Figure S12 (Supporting Information). The pouch cell with a size of 40 × 30 mm was protected by a ≈25  $\mu$ m thick agarose layer, which is thin enough to quickly disintegrate but still thick enough to physically support and protect the remaining battery materials from the surroundings/environment during operation.

Figure 7 shows the optical photographs of the degradation behavior of the different battery components, including the anode, the hydrogel electrolyte, the cathode, and the packaging, over a composting period of 9 weeks. For these experiments, three pouch cells were buried in the soil. After different composting times, each pouch cell was removed from the soil, disassembled, and every battery component was carefully cleaned to reveal its degradation state. After an initial quick browning and deformation of the Zn anode, the hydrogel electrolyte, and the agarose casing, the fragmentation processes of the hydrogel and agarose packaging started at week 2 due to water absorption and hydrolytic degradation reactions.<sup>[70]</sup> Figure S13 (Supporting Information) summarizes the degree of disintegration according to Equation S4 (Supporting Information), showing that the pouch cell continuously disintegrated at a rate of 0.89 wt% per week and lost 49.9 ± 2.9 wt% of its mass after 63 days. Such degradation rate is comparable

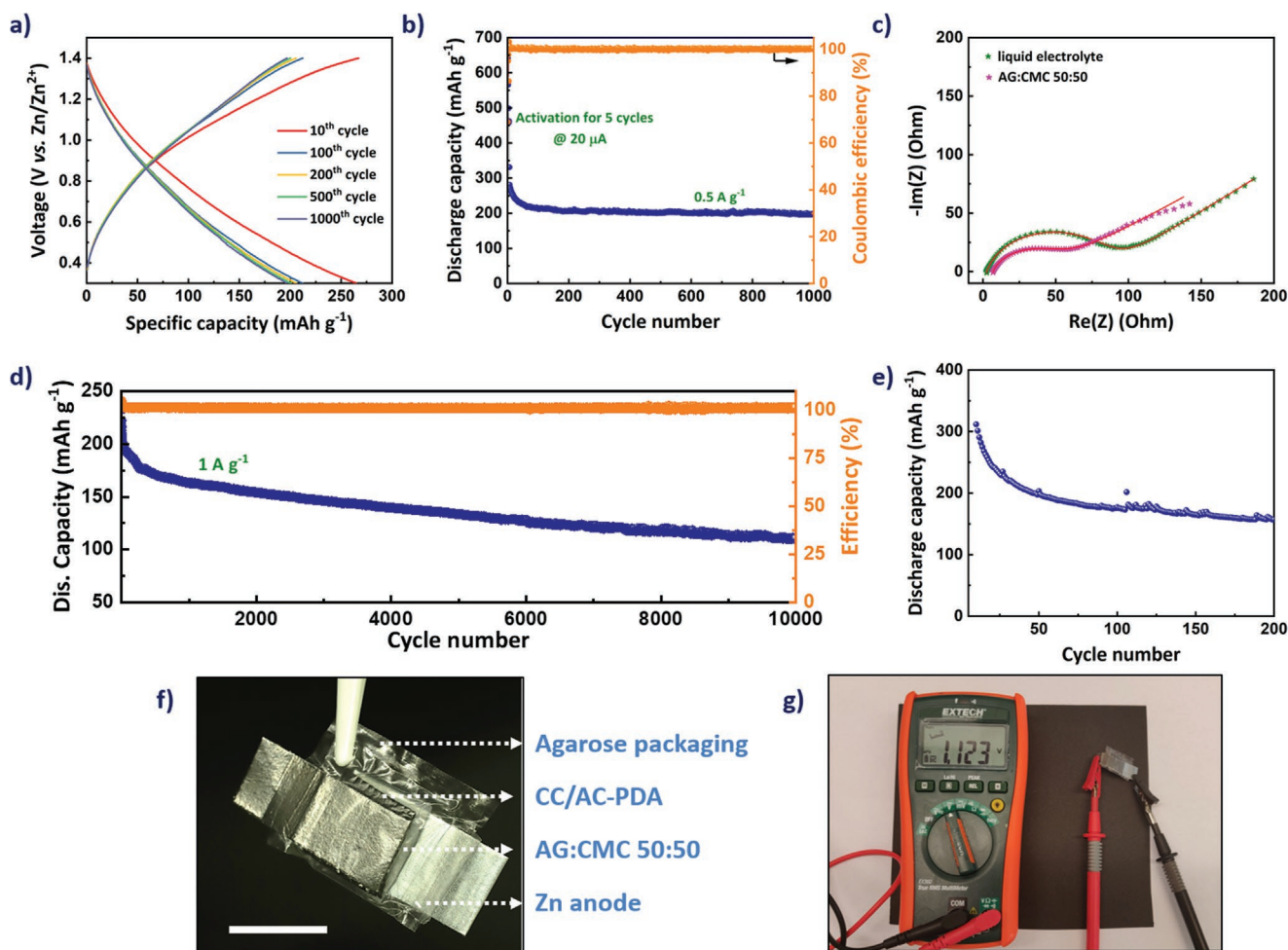


**Figure 6.** Electrochemical performance of the Zn-ion battery (ZIB) composed of a Zn anode, CC-AC/PDA cathode, and AG:CMC 50:50 hydrogel electrolyte: a) galvanostatic charge–discharge profiles at  $0.5 \text{ A g}^{-1}$  along with its corresponding b) cycling performance over 1000 cycles. c) EIS spectra of the ZIBs with the glass fiber-liquid electrolyte and the hydrogel electrolyte. d) Long-term cycling performance at  $1 \text{ A g}^{-1}$  over 10'000 cycles. The characterization of the fabricated pouch cell using Zn anode, CC-AC/PDA cathode, AG:CMC 50:50 hydrogel electrolyte, and agarose packaging: e) cycling performance at  $50 \text{ mA g}^{-1}$ ; f) digital photograph; and g) open-circuit voltage. The scale bar in Figure (f) is 1 cm.

to that of biodegradable and compostable polymers such as poly(butylene succinate-co-adipate) with a 62 wt% mass loss in 140 days,<sup>[71]</sup> or polylactide with nearly 65 wt% mass loss in 63 days,<sup>[72]</sup> highlighting the suitable degradability of the developed transient ZIB.

From an environmental perspective, it is critical that the battery decomposes into harmless secondary products. Therefore, we will discuss below the possible decomposition mechanisms of the individual battery components, their products, and the potential impact on the environment. Battery degradation starts with the agarose casing, which first swells and then hydrolyzes into the simplest sugar units, 3,6-anhydro-L-galactose and D-galactose.<sup>[73]</sup> As the casing continues to degrade, the internal battery components also become corroded. As a transient metal, the zinc anode degrades into  $\text{ZnO}$  and  $\text{Zn(OH)}_2$ .<sup>[74]</sup> This process is relatively rapid compared to other transition metals such as Mo or Fe. On the cathode side, the porous structure of the CC, which we used as the current collector, facilitates the penetration of the moisture, boosting the degradation of PDA into

noncytotoxic derivatives.<sup>[75]</sup> Although the carbon mesh itself keeps its structure intact and shows no signs of degradation, this is not a problem as carbon is considered a nontoxic element and no environmental burdens are expected to arise from the remaining cathode components. Next, the hydrogel electrolyte is broken down into simple water-soluble sugars.<sup>[76]</sup> Glutaraldehyde cross-linker may not be an issue either as it easily degrades under aerobic conditions in the soil, does not bioaccumulate in aquatic organisms, and can be rapidly metabolized in a water-sediment system.<sup>[77]</sup> However,  $\text{ZnSO}_4$  should be considered in an end-of-life scenario because it is toxic to aquatic life (H400 and H410 GHS Hazard statement) and a dose of  $250 \text{ mg kg}^{-1}$  shows acute toxicity in mice.<sup>[78]</sup> The AG:CMC 50:50 hydrogel electrolyte in our pouch cell contains  $322.9 \text{ mg}$  of  $\text{ZnSO}_4$ .

Compared to conventional LIBs, which are designed to last as long as possible, our battery can simply disintegrate without leaving any toxic products behind. Since it consists of harmless and inexpensive materials, it is a promising alternative

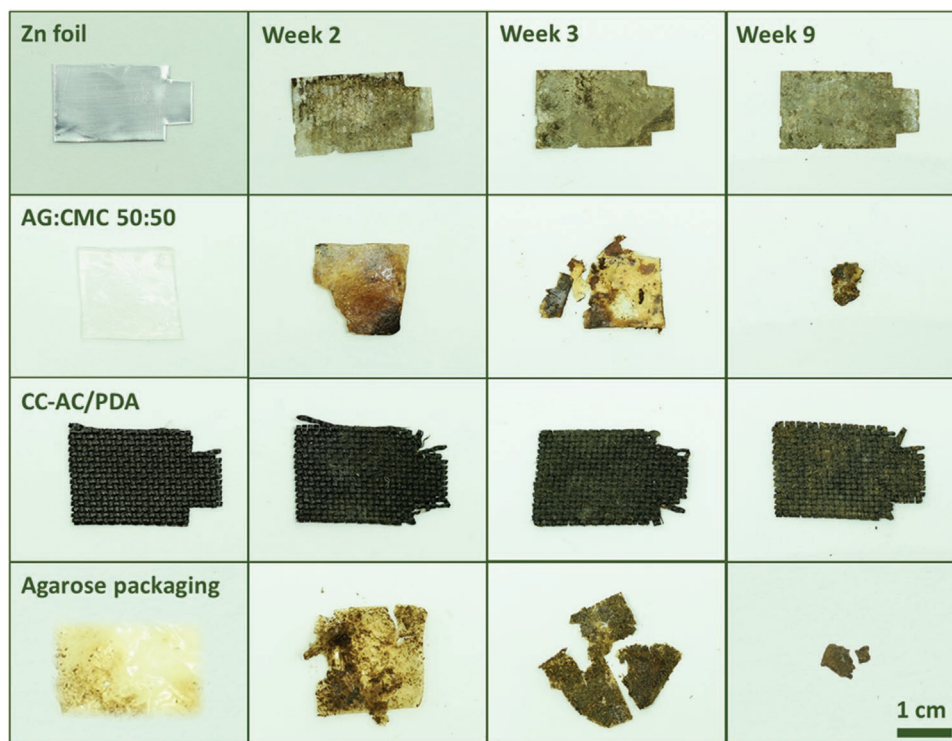


**Figure 7.** Digital photographs showing the degradation behavior of individual battery components of the transient battery after different times under simulating composting conditions at 58 °C.

that, unlike LIBs, does not cause damage to the environment, does not contain expensive elements, and thus does not need to be recycled at great expense. The designed battery also represents an environmentally friendly alternative to current ZIBs, which mostly use nondegradable glass fiber separator and toxic inorganic cathodes. In addition to the excellent decomposition rate of the pouch cell, which makes the transient concept a success, the battery prototype can provide an open-circuit voltage of 1.123 V and deliver a discharge capacity of 157 mAh g<sup>-1</sup> after 200 cycles at a current density of 50 mA g<sup>-1</sup> (Figure 6e–g), sufficient to power electronic components with low power consumption. The observed discharge capacity is only slightly lower than that of the zinc-ion battery tested in Swagelok-type configuration at a current density of 50 mA g<sup>-1</sup>, which is probably due to the poorer interfacial contact between the battery components.

Finally, we also quantified the “cradle-to-gate” environmental impact of the pouch cell fabrication according to life cycle assessment (LCA) to provide further insight into the environmental impact of the transient ZIB. The raw material extraction, the synthesis of different battery components including cathode, anode, biopolymer electrolyte, and the manufacturing of the pouch cell with the packaging were considered. For the sake of transparency, the complete material and energy input inventory is disclosed in Table S3 (Supporting Information). Due to the laboratory-scale character of the pouch cell and the nonoptimized amounts of the anode and cathode, obtained absolute impacts do not provide means for comparison with related systems such as Na-ion batteries,<sup>[79]</sup> or Li-S batteries,<sup>[80]</sup> which present “cradle-to-gate” global warming potential values

of 140.3 and 1274 kg CO<sub>2</sub> equiv. kWh<sup>-1</sup>, respectively. However, a detailed analysis of the distribution of the environmental impact of each battery component can provide guidance for future designs of ZIBs with a low environmental footprint. Figure S14 (Supporting Information) demonstrates that the energy consumption from oven drying (88.3% of the whole energy required) represents the largest environmental impact in 15 of the analyzed categories. In particular, the materials used to fabricate such a transient battery make a remarkably small contribution to the impact categories of fossil resource and mineral resource scarcity (highlighting the circularity of the selected materials), marine and freshwater eco-toxicity, global warming (where energy consumption accounts for 94.9%), ionizing radiation, human carcinogenic toxicity, and freshwater eutrophication. Future improvements can arise from the replacement of ZnSO<sub>4</sub> as it makes a considerable contribution to the category of terrestrial eco-toxicity, while ethanol, piperidine, and CC mainly contribute to marine eutrophication due to the energy and nitrogen required for carbonization under the inert atmosphere.<sup>[81]</sup> In any case, it is essential to mention that the impact of our battery can be reduced by 2 to 25 times depending on the category by optimizing the energy consumption.<sup>[82]</sup> Moreover, it should be considered that our laboratory-scale approach used a 20 L oven to dry samples that have a weight of less than 1 g. Therefore, we estimate that pilot-scale manufacturing would notably lower the environmental footprint of our transient battery. Altogether, these results highlight the environmentally benign character of ZIBs, which do not require toxic organic electrolytes, use earth-abundant materials, and can be assembled under an ambient atmosphere.



### 3. Conclusions

We present a carefully tailored bottom-up design of a zinc-ion battery that combines both excellent transient properties with outstanding electrochemical performance. The battery consists of a biopolymeric hydrogel electrolyte based on environmentally friendly polysaccharides, a zinc anode, and a biocompatible PDA-based cathode. A polysaccharide-based shell makes it possible to control the degradation of the battery, which is vital to maintain its functionality for as long as desired. The reasons for the stable operation of the battery, and in particular the Zn anode, are the favorable interface between metallic Zn and the hydrogel electrolyte, which comes from the hydroxyl-containing functional groups, the mechanical adaptability of the hydrogel, and its excellent ionic conductivity ( $87.57 \times 10^{-3} \text{ S cm}^{-1}$ ) that allows optimal transport of zinc ions. The cathode was systematically improved by depositing PDA directly on a porous carbon substrate as a current collector by the chemical oxidation of dopamine. This carefully tuned battery design showcases a long-term cyclability of over 10'000 cycles at a high current density. In addition, the complete battery exhibits a pronounced transiency under composting conditions as evidenced by the weight loss of  $49.9 \pm 2.9 \text{ wt}\%$  after 63 days. No environmental burden arising from the degradation products or the remaining battery components is expected. Also, all battery components have good environmental performance, resulting in a low environmental impact contribution of the selected materials to the overall footprint, according to a “cradle-to-gate” analysis. With this prototype, a transient battery is now available that also fulfills the full function of an energy storage device from the electrochemical side.

### Supporting Information

Supporting Information is available from the Wiley Online Library or from the author.

### Acknowledgements

The authors gratefully acknowledge financial support from ETH Zurich (ETH Research Grant ETH-45 18-1) and from the Global Training program of the Basque Government. Financial support from the “2021 Euskampus Missions 1.0. Programme” granted by Euskampus Fundazioa is acknowledged. D.K. acknowledges the UNSW for the support through the academic start-up grant. Xavier Aeby from Cellulose and Wood Materials Laboratory, EMPA, is thanked for his support in the degradation experiments. The authors also acknowledge support from the Scientific Center for Optical and Electron Microscopy (ScopeM) of ETH Zurich.

### Conflict of Interest

The authors declare no conflict of interest.

### Data Availability Statement

The data that support the findings of this study are available from the corresponding author upon reasonable request.

### Keywords

aqueous electrolytes, biopolymers, degradation, green batteries, hydrogel electrolytes, transiency, zinc-ion batteries

Received: November 2, 2022  
Published online: November 27, 2022

- [1] M. Arbabzadeh, R. Sioshansi, J. X. Johnson, G. A. Keoleian, *Nat. Commun.* **2019**, *10*, 3413.
- [2] G. Crabtree, *Science* **2019**, *366*, 422.
- [3] European Commission, “Energy storage”, [https://energy.ec.europa.eu/topics/research-and-technology/energy-storage\\_en](https://energy.ec.europa.eu/topics/research-and-technology/energy-storage_en) (accessed: September 2022).
- [4] A. B. Gallo, J. R. Simões-Moreira, H. K. M. Costa, M. M. Santos, E. Moutinho dos Santos, *Renewable Sustainable Energy Rev.* **2016**, *65*, 800.
- [5] M.-M. Titirici, *Adv. Energy Mater.* **2021**, *11*, 2003700.
- [6] X. Aeby, A. Poulin, G. Siqueira, M. K. Hausmann, G. Nyström, *Adv. Mater.* **2021**, *33*, 2101328.
- [7] L. A. Wehner, N. Mittal, T. Liu, M. Niederberger, *ACS Cent. Sci.* **2021**, *7*, 231.
- [8] J. Piątek, S. Afyon, T. M. Budnyak, S. Budnyk, M. H. Sipponen, A. Slabon, *Adv. Energy Mater.* **2020**, *11*, 2003456.
- [9] G. Harper, R. Sommerville, E. Kendrick, L. Driscoll, P. Slater, R. Stolkin, A. Walton, P. Christensen, O. Heidrich, S. Lambert, A. Abbott, K. Ryder, L. Gaines, P. Anderson, *Nature* **2019**, *575*, 75.
- [10] A. Manhart, R. Vogt, M. Priester, G. Dehoust, A. Auberger, M. Blepp, P. Dolega, C. Kämper, J. Giegrich, G. Schmidt, J. Kosmol, *Miner. Econ.* **2019**, *32*, 91.
- [11] D. L. Thompson, J. M. Hartley, S. M. Lambert, M. Shiref, G. D. J. Harper, E. Kendrick, P. Anderson, K. S. Ryder, L. Gaines, A. P. Abbott, *Green Chem.* **2020**, *22*, 7585.
- [12] Y. Liang, H. Dong, D. Aurbach, Y. Yao, *Nat. Energy* **2020**, *5*, 646.
- [13] J. Liu, C. Xu, Z. Chen, S. Ni, Z. X. Shen, *Green Energy Environ.* **2018**, *3*, 20.
- [14] E. Van Genderen, M. Wildnauer, N. Santero, N. Sidi, *Int J Life Cycle Assess* **2016**, *21*, 1580.
- [15] X.-Y. Lou, Z. Xu, A.-P. Bai, M. Resina-Gallego, Z.-G. Ji, *Membranes* **2020**, *10*, 19.
- [16] H. Glatz, E. Lizundia, F. Pacifico, D. Kundu, *ACS Appl. Energy Mater.* **2019**, *2*, 1288.
- [17] L. E. Blanc, D. Kundu, L. F. Nazar, *Joule* **2020**, *4*, 771.
- [18] N. Mittal, A. Ojanguren, M. Niederberger, E. Lizundia, *Adv. Sci.* **2021**, *8*, 2004814.
- [19] C. Clarke, I. D. Williams, D. A. Turner, *Resour., Conserv. Recycl.* **2019**, *141*, 465.
- [20] J. Bae, Y. Li, J. Zhang, X. Zhou, F. Zhao, Y. Shi, J. B. Goodenough, G. Yu, *Angew. Chem., Int. Ed.* **2018**, *57*, 2096.
- [21] A. Naveed, H. Yang, J. Yang, Y. Nuli, J. Wang, *Angew. Chem., Int. Ed.* **2019**, *58*, 2760.
- [22] A. Bani Hashemi, G. Kasiri, F. La Mantia, *Electrochim. Acta* **2017**, *258*, 703.
- [23] Z. Zhao, J. Zhao, Z. Hu, J. Li, J. Li, Y. Zhang, C. Wang, G. Cui, *Energy Environ. Sci.* **2019**, *12*, 1938.
- [24] B. Li, J. Xue, X. Lv, R. Zhang, K. Ma, X. Wu, L. Dai, L. Wang, Z. He, *Surf. Coat. Technol.* **2021**, *421*, 127367.
- [25] C. Huang, X. Zhao, Y. Xu, Y. Zhang, Y. Yang, A. Hu, Q. Tang, X. Song, C. Jiang, X. Chen, *ACS Sustainable Chem. Eng.* **2020**, *8*, 16028.
- [26] S. Y. Liew, J. C. Juan, C. W. Lai, G. T. Pan, T. C. K. Yang, T. K. Lee, *Ionic* **2019**, *25*, 1291.
- [27] J. Liu, S. Willför, C. Xu, *Bioact. Carbohydr. Diet. Fibre* **2015**, *5*, 31.

- [28] A. Ojanguren, N. Mittal, E. Lizundia, M. Niederberger, *ACS Appl. Mater. Interfaces* **2021**, *13*, 21250.
- [29] X. Casas, M. Niederberger, E. Lizundia, *ACS Appl. Mater. Interfaces* **2020**, *12*, 29264.
- [30] N. Reddy, R. Reddy, Q. Jiang, *Trends Biotechnol.* **2015**, *33*, 362.
- [31] E. Lizundia, E. Meaurio, J. M. Laza, J. L. Vilas, L. M. León Isidro, *Mater. Sci. Eng., C* **2015**, *50*, 97.
- [32] H. Khani, S. Kalami, J. B. Goodenough, *Sustainable Energy Fuels* **2019**, *4*, 177.
- [33] M. L. H. Rozali, Z. Ahmad, M. I. N. Isa, *Adv. Mater.* **2015**, *1107*, 223.
- [34] M. Ghelichi, N. T. Qazvini, S. H. Jafari, H. A. Khonakdar, Y. Farajollahi, C. Scheffler, *J. Appl. Polym. Sci.* **2013**, *129*, 1868.
- [35] S. M. Ibrahim, K. M. El Salmawi, *J. Polym. Environ.* **2013**, *21*, 520.
- [36] S. A. Foord, E. D. Y. Atkins, *Biopolymers* **1989**, *28*, 1345.
- [37] I. Gholamali, *Regener. Eng. Transl. Med.* **2020**, *6*, 115.
- [38] A. M. Hyde, S. L. Zultanski, J. H. Waldman, Y. L. Zhong, M. Shevlin, F. Peng, *Org. Process Res. Dev.* **2017**, *21*, 1355.
- [39] S. Kiruthika, M. Malathi, S. Selvasekarapandian, K. Tamilarasan, V. Moniha, R. Manjuladevi, *J. Solid State Electrochem.* **2019**, *23*, 2181.
- [40] T. Mlčoch, J. Kučerík, *J. Therm. Anal. Calorim.* **2013**, *113*, 1177.
- [41] M. El-Sakhawy, H. A. S. Tohamy, A. Salama, S. Kamel, *Cellul. Chem. Technol.* **2019**, *53*, 667.
- [42] P. D. Haller, L. C. Bradley, M. Gupta, *Langmuir* **2013**, *29*, 11640.
- [43] D. Yuan, W. Manalastas, L. Zhang, J. J. Chan, S. Meng, Y. Chen, M. Srinivasan, *ChemSusChem* **2019**, *12*, 4889.
- [44] S. Zhang, N. Yu, S. Zeng, S. Zhou, M. Chen, J. Di, Q. Li, *J. Mater. Chem. A* **2018**, *6*, 12237.
- [45] Y. Ma, X. Xie, R. Lv, B. Na, J. Ouyang, H. Liu, *ACS Sustainable Chem. Eng.* **2018**, *6*, 8697.
- [46] L. Porcarelli, A. S. Shaplov, F. Bella, J. R. Nair, D. Mecerreyes, C. Gerbaldi, *ACS Energy Lett.* **2016**, *1*, 678.
- [47] J. Evans, C. A. Vincent, P. G. Bruce, *Polymer* **1987**, *28*, 2324.
- [48] P. G. Bruce, M. T. Hardgrave, C. A. Vincent, *Solid State Ionics* **1992**, *53*, 1087.
- [49] M. Gouverneur, F. Schmidt, M. Schönhoff, *Phys. Chem. Chem. Phys.* **2018**, *20*, 7470.
- [50] Q. Yang, F. Mo, Z. Liu, L. Ma, X. Li, D. Fang, S. Chen, S. Zhang, C. Zhi, *Adv. Mater.* **2019**, *31*, 1901521.
- [51] A. B. Lindstrom, M. J. Strynar, E. L. Libelo, *Environ. Sci. Technol.* **2011**, *45*, 7954.
- [52] L. Ma, C. Zhi, *Electrochem. Commun.* **2021**, *122*, 106898.
- [53] S. O. Tung, S. Ho, M. Yang, R. Zhang, N. A. Kotov, *Nat. Commun.* **2015**, *6*, 6152.
- [54] C. M. Walters, G. K. Matharu, W. Y. Hamad, E. Lizundia, M. J. MacLachlan, *Chem. Mater.* **2021**, *33*, 5197.
- [55] D. Ye, C. Chang, L. Zhang, *Biomacromolecules* **2019**, *20*, 1989.
- [56] P. Barai, K. Higa, V. Srinivasan, *Phys. Chem. Chem. Phys.* **2017**, *19*, 20493.
- [57] M. Zhu, X. Wang, H. Tang, J. Wang, Q. Hao, L. Liu, Y. Li, K. Zhang, O. G. Schmidt, *Adv. Funct. Mater.* **2020**, *30*, 1907218.
- [58] Q. Zhang, J. Luan, L. Fu, S. Wu, Y. Tang, X. Ji, H. Wang, *Angew. Chem., Int. Ed.* **2019**, *58*, 15841.
- [59] L. Wang, Y. Zhang, H. Hu, H. Y. Shi, Y. Song, D. Guo, X. X. Liu, X. Sun, *ACS Appl. Mater. Interfaces* **2019**, *11*, 42000.
- [60] Y. Tian, Y. An, C. Wei, B. Xi, S. Xiong, J. Feng, Y. Qian, *ACS Nano* **2019**, *13*, 11676.
- [61] Y. Mao, H. Ren, J. Zhang, T. Luo, N. Liu, B. Wang, S. Le, N. Zhang, *Electrochim. Acta* **2021**, *393*, 139094.
- [62] Y. K. Jeong, S. H. Park, J. W. Choi, *ACS Appl. Mater. Interfaces* **2018**, *10*, 7562.
- [63] C. Cao, L. Tan, W. Liu, J. Ma, L. Li, *J. Power Sources* **2014**, *248*, 224.
- [64] I. You, H. Jeon, K. Lee, M. Do, Y. C. Seo, H. A. Lee, H. Lee, *J. Ind. Eng. Chem.* **2017**, *46*, 379.
- [65] Z. Wang, K. K. Fu, Z. Liu, Y. Yao, J. Dai, Y. Wang, B. Liu, L. Hu, *Adv. Funct. Mater.* **2017**, *27*, 1605724.
- [66] K. Fu, Z. Liu, Y. Yao, Z. Wang, B. Zhao, W. Luo, J. Dai, S. D. Lacey, L. Zhou, F. Shen, M. Kim, L. Swafford, L. Sengupta, L. Hu, *Nano Lett.* **2015**, *15*, 4664.
- [67] K. Fu, Z. Wang, C. Yan, Z. Liu, Y. Yao, J. Dai, E. Hitz, Y. Wang, W. Luo, Y. Chen, M. Kim, L. Hu, *Adv. Energy Mater.* **2016**, *6*, 1502496.
- [68] N. Mittal, A. Ojanguren, N. Cavin, E. Lizundia, M. Niederberger, *Adv. Funct. Mater.* **2021**, *31*, 2101827.
- [69] J.-W. Rhim, *J. Food Sci.* **2012**, *77*, N66.
- [70] K. Fukushima, D. Tabuani, C. Abbate, M. Arena, L. Ferreri, *Polym. Degrad. Stab.* **2010**, *95*, 2049.
- [71] A. Larrañaga, E. Lizundia, *Eur. Polym. J.* **2019**, *121*, 109296.
- [72] Y. Luo, Z. Lin, G. Guo, *Nanoscale Res. Lett.* **2019**, *14*, 56.
- [73] S. S. Sawant, B. K. Salunke, L. E. Taylor, B. S. Kim, *Appl. Sci.* **2017**, *7*, 225.
- [74] L. Yin, H. Cheng, S. Mao, R. Haasch, Y. Liu, X. Xie, S.-W. Hwang, H. Jain, S.-K. Kang, Y. Su, R. Li, Y. Huang, J. A. Rogers, *Adv. Funct. Mater.* **2014**, *24*, 645.
- [75] R. Batul, T. Tamanna, A. Khaliq, A. Yu, *Biomater. Sci.* **2017**, *5*, 1204.
- [76] C. Jiang, Z. Liu, D. Cheng, X. Mao, *Biotechnol. Adv.* **2020**, *45*, 107641.
- [77] U.S. Department of Health and Human Services, *Toxicological Profile for Glutaraldehyde*, July **2017**.
- [78] C. Wang, K. Cheng, L. Zhou, J. He, X. Zheng, L. Zhang, X. Zhong, T. Wang, *Biol. Trace Elem. Res.* **2017**, *178*, 276.
- [79] J. Peters, D. Buchholz, S. Passerini, M. Weil, *Energy Environ. Sci.* **2016**, *9*, 1744.
- [80] S. Lopez, O. Akizu-Gardoki, E. Lizundia, *J. Cleaner Prod.* **2021**, *282*, 124528.
- [81] J. F. Peters, A. P. Cruz, M. Weil, *Batteries* **2019**, *5*, 10.
- [82] E. G. Hertwich, T. Gibon, E. A. Bouman, A. Arvesen, S. Suh, G. A. Heath, J. D. Bergesen, A. Ramirez, M. I. Vega, L. Shi, *Proc. Natl. Acad. Sci. USA* **2015**, *112*, 6277.